

Impact of lensing bias on the cosmological dispersion measure

Ryuichi Takahashi

Faculty of Science and Technology, Hirosaki University, 3 Bunkyo-cho, Hirosaki, Aomori 036-8561, Japan

Abstract. The cosmological dispersion measure (DM) as a function of redshift, derived from localized fast radio bursts (FRBs), has been used as a tool for constraining the cosmic ionized fraction and cosmological parameters. For these purposes, the DM in a homogeneous cosmological model has typically been used, neglecting the inhomogeneity of matter distribution. In this study, we derive a bias in the ensemble average of the DM over many FRBs owing to gravitational lensing by the inhomogeneous matter distribution based on cosmological perturbation theory. We demonstrate that the ensemble average is 0.4%–1% smaller than the DM in the corresponding homogeneous model for a source redshift of $z_s = 1$, according to recent cosmological hydrodynamic simulations of IllustrisTNG and BAHAMAS. This reduction occurs because light rays from FRBs tend to avoid high-density regions owing to lensing deflection. We also discuss another selection effect, magnification bias, where demagnified FRBs with low DMs, fainter than the detection threshold, are excluded from the observed sample, leading to a selective observation of magnified FRBs with high DMs. Lensing bias, including magnification bias, must be considered to achieve percent level accuracy in the DM–redshift relation.

Contents

1	Introduction	1
2	Ensemble average of the DM	3
2.1	Light ray path in an inhomogeneous universe	3
2.2	The DM in an inhomogeneous universe	4
2.3	The cross-power spectrum of matter and free electrons	5
3	Results	8
4	Magnification bias	10
5	Discussion	11
5.1	The other second-order effects on $\langle \text{DM} \rangle$	11
5.2	Rotation measure	12
6	Conclusions	12
A	Derivation of the DM correction terms	19
B	Free-electron bias	21

1 Introduction

Fast radio burst (FRB) is a radio transient, with a typical duration of milliseconds, from a cosmological distance (e.g., recent reviews [1–4]). Many theoretical models for FRBs have been proposed, but their physical origin is still elusive (e.g., [4]). From a frequency dependence of the arrival time, the dispersion measure (DM) is measured, which is the column density of free electrons along the light path to the source. If its host galaxy is identified, it is called a localized FRB, and its redshift can be determined. Currently, at least 40 localized FRBs have been identified (e.g., [5–11]), with the highest redshift being $z_s = 1.0$ [12]. The observed DM is influenced by contributions from the Milky Way (MW), the host galaxy, and cosmological objects such as the inter-galactic medium (IGM) and intervening galaxies. Because the cosmological contribution is dominant for relatively high source redshifts ($z_s \gtrsim 0.5$), we focus solely on the cosmological DM in this study.

The DM–redshift relation, measured from localized FRBs, has been utilized to constrain the ionized fraction in the IGM (f_e) [13–17], Hubble parameter (H_0) [18–24], and cosmic baryon abundance (Ω_b) [5, 25, 26]. Because these parameters are completely degenerate ($\text{DM} \propto H_0 f_e \Omega_b$), external constraints or assumptions are required to determine one of them. When many localized FRBs are available at high redshifts ($z_s \gtrsim 0.5$), the DM– z relation can probe the properties of dark energy (e.g., [27–29]) and the history of cosmic reionization (e.g., [30–35]). In all previous works, the DM was calculated using a homogeneous cosmological model. In this study, we investigate the effects of matter inhomogeneity on the ensemble average of the DM over many FRBs.

The effects of inhomogeneous mass distribution on the luminosity distance D_L have been extensively studied for supernova (SN) cosmology, utilizing second-order cosmological

perturbation theory (e.g., [36–47]; also the recent review [48]). Matter inhomogeneity causes a scatter and a bias in D_L . The bias arises from the second-order term of density fluctuations because the first-order term averages out over many sources. For high redshifts ($z_s \gtrsim 0.3$), the dominant contribution is gravitational lensing, while for low redshifts ($z_s \lesssim 0.3$), it is the peculiar motions of the observer and the source [39, 40]. In this study, we focus on the lensing contribution, with other second-order effects briefly discussed in Subsection 5.1. The ensemble average of D_L in an inhomogeneous universe, $\langle D_L \rangle$, and that in the corresponding homogeneous model, \bar{D}_L , follow a simple relation: $\langle D_L \rangle = [1 + (3/2)\langle \kappa^2 \rangle]\bar{D}_L$, where κ is the convergence field (e.g., [44, 49]). Given that the variance of κ is estimated as $\langle \kappa^2 \rangle \approx (2-8) \times 10^{-3} z_s^2$ [50–53], the lensing bias increases D_L by $\mathcal{O}(0.1\%–1\%)$ for $z_s \gtrsim 0.4$. This bias will need to be accounted for in future SN cosmology analyses (e.g., [36, 54]).

Kaiser & Peacock (2016) [44] (hereafter KP16) evaluated the lensing bias in $\langle D_L \rangle$ using standard perturbation theory. By solving the null-geodesic equation, they demonstrated that light rays propagate through underdense regions on average because they tend to avoid matter clumps owing to lensing deflection. They also analytically derived that the average convergence κ is negative, satisfying the simple relation $\langle \kappa \rangle = -2\langle \kappa^2 \rangle$. This originates from flux conservation¹ [55]. This relation is also confirmed by cosmological ray-tracing simulations [56] and for weak lensing of gravitational waves in wave optics (i.e., without the geometrical-optics approximation) [57, 58].

In this study, we calculate the lensing bias in the average of the DM, $\langle \text{DM} \rangle$, in an inhomogeneous universe where the total matter (dark matter and baryons) and free-electron distributions are inhomogeneous. A standard deviation of the DM caused by matter inhomogeneity has been previously studied (e.g., [59–63]), but the bias has not yet been examined. We use the standard cosmological perturbation theory following the KP16 procedure. Based on previous studies on $\langle D_L \rangle$, we expect $\langle \text{DM} \rangle$ to be smaller than the prediction from the homogeneous model. Section 2 details our approach, where we integrate the free-electron density along null geodesics in curved spacetime to compute the DM and then expand it in terms of density fluctuations. We derive a leading correction term in $\langle \text{DM} \rangle$ determined by the cross-power spectrum of matter and free electrons (Appendix A), utilizing data from recent hydrodynamic simulations of IllustrisTNG² and BAHAMAS³. Section 3 presents numerical results for $\langle \text{DM} \rangle$, comparing it with predictions from the homogeneous model. We also discuss the influence of baryonic feedback on $\langle \text{DM} \rangle$. Section 4 addresses another selection effect, magnification bias, and its impact on $\langle \text{DM} \rangle$. Section 5 discusses other second-order effects aside from lensing bias (Subsection 5.1) and provides insights into lensing bias in rotation measures (Subsection 5.2). Finally, Section 6 summarizes the findings of this study.

In this paper, for any arbitrary quantity f , $\langle f \rangle$ denotes its ensemble average in an inhomogeneous universe, while \bar{f} represents its value in the corresponding homogeneous model. We adopt a spatially flat Λ CDM model consistent with the *Planck* 2015 best-fitting parameters [64]: matter density $\Omega_m = 1 - \Omega_\Lambda = 0.3089$, baryon density $\Omega_b = 0.0486$, Hubble parameter $h = 0.6774$, spectral index $n_s = 0.9667$, and amplitude of matter density fluctuations on the scale of $8 h^{-1} \text{Mpc}$ $\sigma_8 = 0.8159$. This model is identical to the one used in IllustrisTNG. All physical quantities such as length, wavenumber, and number density are

¹From flux conservation, the average lensing magnification is unity, $\langle \mu \rangle = 1$. Using $\mu = 1/[(1 - \kappa)^2 - \gamma^2]$ (γ is the shear field, satisfying $\langle \gamma^2 \rangle = \langle \kappa^2 \rangle$) with $|\kappa|, |\gamma| \ll 1$, one obtains $\langle \kappa \rangle = -2\langle \kappa^2 \rangle$. Similarly, the bias in D_L is obtained as $\langle D_L \rangle = \langle \mu^{-1/2} \rangle \bar{D}_L \simeq [1 + (3/2)\langle \kappa^2 \rangle]\bar{D}_L$.

²<https://www.tng-project.org/>

³<https://www.astro.ljmu.ac.uk/~igm/BAHAMAS/>

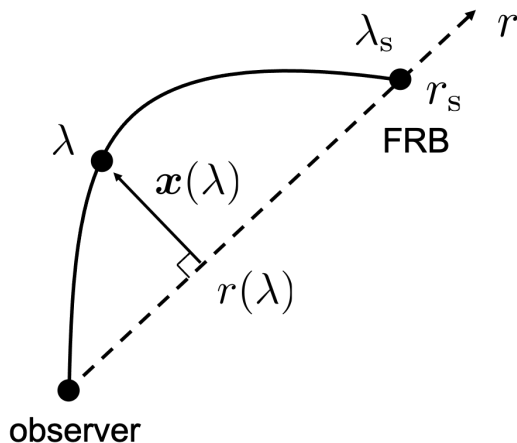


Figure 1. The solid curve represents the path of a light ray toward the FRB, parameterized by the affine parameter (path length) λ : $\lambda = 0$ at the observer and $\lambda = \lambda_s$ at the source. The dashed line represents the radial coordinate r toward the source, and \mathbf{x} denotes a two-dimensional coordinate perpendicular to the r -axis.

expressed in comoving units.

2 Ensemble average of the DM

2.1 Light ray path in an inhomogeneous universe

This subsection briefly explores the path of a light ray in an inhomogeneous universe (e.g., Appendices of KP16; a review [65]; a textbook [66]). Figure 1 illustrates the coordinate system used. The r axis represents the radial coordinate (comoving distance) connecting the observer and the FRB. The coordinate r is expressed as a function of redshift z : $r(z) = c \int_0^z dz'/H(z')$, where $H(z)$ is the Hubble expansion rate. The distance to the source is $r_s = r(z_s)$. The two-dimensional coordinate \mathbf{x} is perpendicular to the r -axis. The spatial coordinate is denoted by $\mathbf{r} = (r, \mathbf{x})$.

In a homogeneous universe, a light ray from the source travels along the r -axis. In an inhomogeneous scenario, the propagation of a light ray is affected by gravitational deflections caused by matter clumps. The matter inhomogeneity generates a gravitational potential $\phi = \phi(\mathbf{r}; z)$, assuming weak gravity ($|\phi|/c^2 \ll 1$). We adopt the Newtonian gauge for the metric perturbation and neglect the peculiar velocities of the observer and source. The path of a light ray is determined by the geodesic equation with the affine parameter λ : $d^2\mathbf{r}/d\lambda^2 = -(2/c^2)\nabla_{\perp}\phi$ where ∇_{\perp} is derivative in the direction perpendicular to the path. Here, λ is the path length from the observer. The geodesic equation is solved under the boundary condition that the positions at both endpoints are fixed to those of the observer and the source (Appendix E of KP16):

$$\begin{aligned} \frac{d\mathbf{x}}{d\lambda}(\lambda) &= -\frac{2}{c^2} \int_0^{\lambda} d\lambda' \nabla_{\mathbf{x}'} \phi(\mathbf{r}'; z') + \frac{2}{c^2} \frac{1}{\lambda_s} \int_0^{\lambda_s} d\lambda' (\lambda_s - \lambda') \nabla_{\mathbf{x}'} \phi(\mathbf{r}'; z'), \\ \mathbf{x}(\lambda) &= -\frac{2}{c^2} \int_0^{\lambda} d\lambda' (\lambda - \lambda') \nabla_{\mathbf{x}'} \phi(\mathbf{r}'; z') + \frac{2}{c^2} \frac{\lambda}{\lambda_s} \int_0^{\lambda_s} d\lambda' (\lambda_s - \lambda') \nabla_{\mathbf{x}'} \phi(\mathbf{r}'; z'), \end{aligned} \quad (2.1)$$

where $\mathbf{r}' = \mathbf{r}(\lambda') = (r(\lambda'), \mathbf{x}(\lambda'))$, $z' = z(\lambda')$, and $\nabla_{\mathbf{x}}$ ($\simeq \nabla_{\perp}$) is the gradient with respect to \mathbf{x} . Equation (2.1) includes terms up to the first order of ϕ/c^2 . Because the gravitational potential is weak, we obtain $|\mathbf{x}| \ll r$.

A light ray can also experience deflection by an inhomogeneous plasma density caused by spatial variations in the refractive index (plasma lensing). We have disregarded this effect because the deflection angle is typically negligible, except in cases involving high-density clumps at low radio frequencies ν . For lensing by an intervening galaxy, the deflection angle is typically ≈ 1 arcsec for gravitational lensing and $\approx 10^{-3} (\nu/400\text{MHz})^{-2}$ arcsec for plasma lensing (e.g., [67]).

2.2 The DM in an inhomogeneous universe

The DM represents the column density of free electrons along the path to the source⁴ (e.g., [30, 31, 70]):

$$\text{DM}(z_s) = \int_0^{\lambda_s} d\lambda n_e(\mathbf{r}; z) (1 + z). \quad (2.2)$$

The integration is conducted along the geodesic (2.1). The free-electron density n_e is separated into its spatial mean \bar{n}_e and fluctuations δ_e :

$$n_e(\mathbf{r}; z) = \bar{n}_e(z) [1 + \delta_e(\mathbf{r}; z)]. \quad (2.3)$$

The spatial average of the second term vanishes, $\langle \delta_e \rangle = 0$. The mean free-electron number density is expressed as (e.g., [71]):

$$\bar{n}_e(z) = \frac{3H_0^2 \Omega_b}{8\pi G m_p} \left(X(z) + \frac{1}{2}Y(z) \right) f_e(z), \quad (2.4)$$

where m_p is the proton mass, X and Y are the mass fractions of hydrogen and helium ($X \simeq 0.75$ and $Y \simeq 0.25$), and f_e is the ionized fraction ($f_e \approx 0.7\text{--}0.9$). In the homogeneous model, the DM simplifies to

$$\begin{aligned} \overline{\text{DM}}(z_s) &= \int_0^{r_s} dr \bar{n}_e(z) (1 + z), \\ &= \int_0^{z_s} \frac{c dz}{H(z)} \bar{n}_e(z) (1 + z). \end{aligned} \quad (2.5)$$

The integration is done along the r -axis.

Next, we derive a leading correction term in the DM arising from second-order perturbations (ϕ/c^2 and δ_e). In Eq. (2.2), because $|\mathbf{x}| \ll r$, n_e can be expanded up to the linear order of \mathbf{x} :

$$\begin{aligned} n_e(\mathbf{r}; z) &\simeq n_e(\mathbf{r}; z)|_{\mathbf{x}=0} + \mathbf{x} \cdot \nabla_{\mathbf{x}} n_e(\mathbf{r}; z)|_{\mathbf{x}=0}, \\ &= \bar{n}_e(z) [1 + \delta_e(\mathbf{r}; z)|_{\mathbf{x}=0} + \mathbf{x} \cdot \nabla_{\mathbf{x}} \delta_e(\mathbf{r}; z)|_{\mathbf{x}=0}]. \end{aligned} \quad (2.6)$$

⁴The DM- z relation is sometimes referred to as the Macquart relation [25], although it had been developed earlier in previous studies (e.g., [30, 31, 68–71]).

The integral along the geodesic in Eq. (2.2) is replaced by integration along the r -axis:

$$\begin{aligned} d\lambda &= \sqrt{1 + \left(\frac{d\mathbf{x}}{d\lambda}\right)^2}\Big|_{\mathbf{x}=0} dr, \\ &\simeq dr + \frac{1}{2} \left(\frac{d\mathbf{x}}{d\lambda}\right)^2\Big|_{\mathbf{x}=0} dr. \end{aligned} \quad (2.7)$$

Using Eqs. (2.2), (2.6) and (2.7), we derive the ensemble average of the DM as

$$\begin{aligned} \langle \text{DM} \rangle(z_s) &= \int_0^{r_s} dr \bar{n}_e(z) (1+z) + \int_0^{r_s} dr \bar{n}_e(z) (1+z) \langle \mathbf{x} \cdot \nabla_{\mathbf{x}} n_e(\mathbf{r}; z) |_{\mathbf{x}=0} \rangle \\ &\quad + \frac{1}{2} \int_0^{r_s} dr \bar{n}_e(z) (1+z) \left\langle \left(\frac{d\mathbf{x}}{d\lambda}\right)^2\Big|_{\mathbf{x}=0} \right\rangle. \end{aligned} \quad (2.8)$$

The first term corresponds to the DM in the homogeneous model (2.5). The second and third terms represent the leading correction terms. Appendix A provides a detailed calculation of these terms; the second term is negative⁵, whereas the third is positive. Because the third term is $\approx 10^{-7}$ (10^{-5}) times smaller than the first (second) term for $z_s = 0-3$, we disregard the third term in subsequent analysis.

In summary, the ensemble average of the DM is written as

$$\langle \text{DM} \rangle(z_s) = \overline{\text{DM}}(z_s) + \Delta \text{DM}(z_s), \quad (2.9)$$

with

$$\Delta \text{DM}(z_s) = -\frac{3H_0^2 \Omega_m}{2\pi c^2} \int_0^{z_s} \frac{cdz}{H(z)} \bar{n}_e(z) (1+z)^2 \frac{r(z)(r_s - r(z))}{r_s} \int_0^\infty dk_\perp k_\perp P_{\text{me}}(k_\perp; z), \quad (2.10)$$

where P_{me} is the cross-power spectrum of matter and free electrons (defined in Eq. (A.4)); therefore, ΔDM originates from the cross-correlation between these two fields. The distributions of matter and free electrons determine \mathbf{x} and $\nabla_{\mathbf{x}} n_e$, respectively, in Eq. (2.8). Our result (2.9) is consistent with the previous one for the average convergence, $\langle \kappa \rangle = -2\langle \kappa^2 \rangle$, when κ is used instead of the DM (see also Appendix A). According to Eq. (2.10), the density fluctuations approximately halfway to the source (i.e., $r(z) \approx r_s/2$) contribute the most to ΔDM .

2.3 The cross-power spectrum of matter and free electrons

This subsection discusses two theoretical models of P_{me} in Eq. (2.10). The first one is our fitting function of P_{me} based on the hydrodynamic simulations of IllustrisTNG [73–78]. The other is a numerical scheme of HMX⁶ [72, 79] calibrated with another hydrodynamic simulation suite of BAHAMAS [80, 81]. A comparison of these different models helps to understand the baryonic feedback effect on P_{me} .

We measure P_{me} in the public IllustrisTNG data set [78] to make its fitting function, following the same procedure as in our previous work [63] (their Subsection 3.3). The simulations follow the gravitational clustering of matter (dark matter and baryons), as well as

⁵The vector \mathbf{x} points from high to low density, whereas the direction of $\nabla_{\mathbf{x}} n_e$ is the opposite; thus, the second term is negative.

⁶<https://github.com/tilmantroester/pyhmcodes>

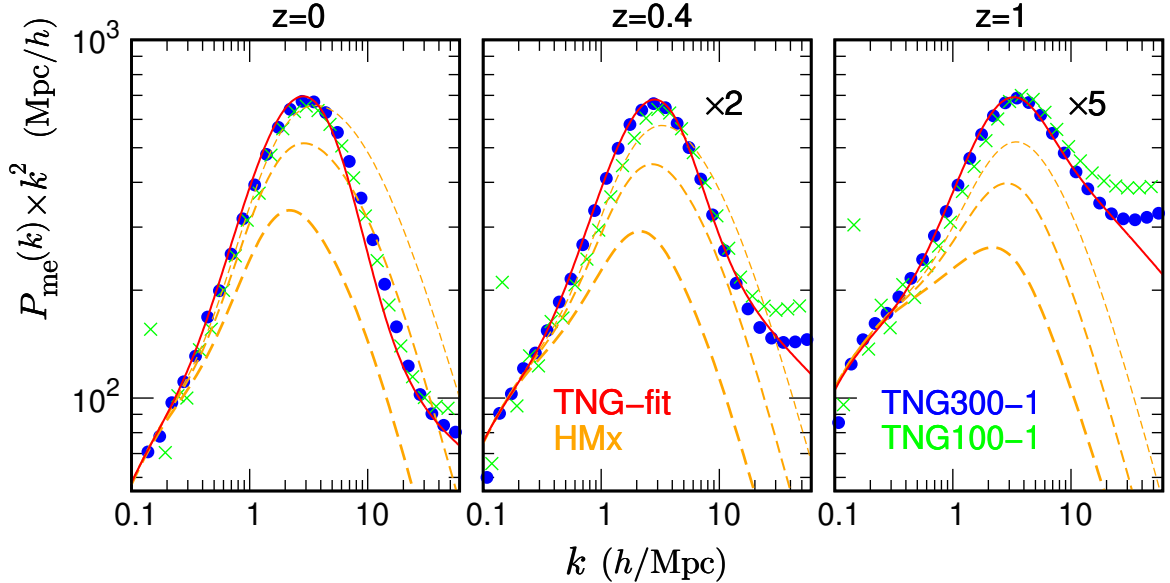


Figure 2. Cross-power spectrum of matter and free electrons at $z = 0, 0.4$, and 1 . The blue and green symbols represent results from hydrodynamic simulations TNG300-1 and TNG100-1, respectively. The red curves depict our theoretical model based on the free-electron bias (2.12) fitted to the TNG results. The dashed orange curves show predictions from HMx [72], calibrated with BAHAMAS. The three orange curves differ in the AGN feedback temperature: $\log_{10}(T_{\text{AGN}}/\text{K}) = 7.6$ (thin), 7.8 (average), and 8.0 (thick), where the higher temperature corresponds to the stronger feedback. In the middle and right panels, the amplitudes are multiplied by 2 and 5, respectively, to make the peak heights uniform.

astrophysical processes such as star and galaxy formation, and stellar and active galactic nucleus (AGN) feedback. The gravitational evolution and magneto-hydrodynamic processes were computed with the moving-mesh code AREPO [82]. We analyzed two simulations with different box sizes: TNG300-1 and TNG100-1. TNG300-1 (TNG100-1) comprises 2500^3 (1820^3) dark matter particles and a nearly equivalent number of baryon particles in a cubic box with a side length of 205 (75) $h^{-1}\text{Mpc}$; thus, TNG100-1 offers higher spatial and mass resolutions. The baryon particles consist of gas, stars, and black holes, with free electrons included in the gas particles. To calculate the matter density contrast δ_{m} , we assign the masses of dark matter and baryon particles to regular grid cells using the cloud-in-cell interpolation with the interlacing scheme (e.g., [83–85]). Similarly, we calculate the free-electron density contrast δ_{e} by assigning the masses of free electrons to the grid cells. Fourier transforms of these density fields, $\tilde{\delta}_{\text{m}}(\mathbf{k})$ and $\tilde{\delta}_{\text{e}}(\mathbf{k})$, are computed using the fast Fourier transform⁷. The power spectrum is then measured as

$$P_{\text{me}}(k; z) = \frac{1}{N_{\text{mode}}} \sum_{|\mathbf{k}'| \in k} \text{Re} \left[\tilde{\delta}_{\text{m}}(\mathbf{k}') \tilde{\delta}_{\text{e}}^*(\mathbf{k}') \right], \quad (2.11)$$

where the summation is performed in the spherical shell $k - \Delta k/2 < |\mathbf{k}'| < k + \Delta k/2$ with a bin width of $\Delta \log_{10} k = 0.1$, and N_{mode} represents the number of Fourier modes in the shell. The power spectrum is reliable up to the particle Nyquist wavenumber k_{Nyq} , determined by

⁷FFTW (Fastest Fourier Transform in the West) at <http://www.fftw.org>.

the mean separation of gas particles $r_{\text{gas}}: k_{\text{Nyq}} = \pi/r_{\text{gas}} = 38.3 (76.2) h \text{ Mpc}^{-1}$ for TNG300-1 (TNG100-1). We measured P_{me} at $z = 0, 0.2, 0.4, 0.7, 1, 2$ and 3 .

The TNG team also conducted dark matter-only (DMO) runs, where the box sizes and the number of dark matter particles matched those in TNG300-1 and TNG100-1, respectively. These runs include N-body particles representing dark matter and baryons, focusing solely on gravitational evolution. We measure the matter power spectra in the DMO runs, denoted as P_{DMO} , using the identical procedure as for P_{me} . Subsequently, we define the free-electron bias:

$$b_e(k; z) \equiv \frac{P_{\text{me}}(k; z)}{P_{\text{DMO}}(k; z)}. \quad (2.12)$$

The fitting function of b_e is detailed in Appendix B. It is worth noting that the free-electron bias (2.12) differs slightly from our previous definition [63], i.e., $b_e^{(\text{prev})}(k; z) \equiv [P_e(k; z)/P_{\text{DMO}}(k; z)]^{1/2}$, where $P_e(k; z)$ is the auto-power spectrum of free electrons. The discrepancy is noticeable only on small scales ($k \gtrsim 1 h \text{ Mpc}^{-1}$), as discussed in Appendix B.

Moving on to HMX, the BAHAMAS simulations were conducted using the smoothed-particle hydrodynamic code GADGET-3 [86], incorporating subgrid models to simulate baryonic processes. The stellar and AGN feedback models were calibrated to match observations of the galaxy’s stellar mass function and the hot gas fraction in galaxy groups and clusters. AGN feedback strength is specified by the heating temperature: $\log_{10}(T_{\text{AGN}}/\text{K}) = 7.6, 7.8,$ and 8.0 where 7.8 is their fiducial value consistent with the observed hot gas fraction of groups and clusters [80]. There are 1024^3 dark matter particles and an equivalent number of baryon particles in a box volume of $(400 h^{-1} \text{ Mpc})^3$. HMX utilizes the halo model framework (e.g., [87–90]), calibrated to reproduce auto- and cross-power spectra of five fields: total matter, cold dark matter, gas, stars, and electron pressure, measured in BAHAMAS. The calibration range is $k = 0.015\text{--}7 h \text{ Mpc}^{-1}$ and $z = 0\text{--}1$. We derive P_{me} from the cross-power spectrum of matter and gas in HMX, denoted as $P_{\text{mg}}^{\text{HMX}}$, assuming that free electrons exactly trace gas (i.e., $\delta_e = \delta n_e/\bar{n}_e = \delta \rho_{\text{gas}}/\bar{\rho}_{\text{gas}}$). Because the normalization of $P_{\text{mg}}^{\text{HMX}}$ differs from our P_{me} , we rescale it⁸. Previously, the HMX power spectrum was used to calculate the covariance of the DM [91] and the angular cross-power spectrum of the DM and κ [92].

Figure 2 presents P_{me} at $z = 0, 0.4,$ and 1 . The blue and green symbols denote TNG measurements. The TNG300-1 and TNG100-1 show consistent results for $k \lesssim 10 h \text{ Mpc}^{-1}$. However, the TNG100-1 gives slightly higher amplitudes for $k \gtrsim 10 h \text{ Mpc}^{-1}$, probably owing to the finer spatial resolution. The red curves are our theoretical model, $P_{\text{me}}(k; z) = b_e(k; z)P_{\text{DMO}}(k; z)$, using the fitting function of b_e and HALOFIT [93, 94] for the non-linear matter power spectrum P_{DMO} . The dashed orange curves are the HMX results. All TNG and HMX results agree at the largest scale ($k < 1 h \text{ Mpc}^{-1}$) because the free electrons trace the underlying dark matter irrespective of baryonic physics [63]. The free-electron bias is almost unity at such a large scale (Appendix B). For $k > 1 h \text{ Mpc}^{-1}$, P_{me} shows suppression influenced by AGN feedback strength; higher T_{AGN} leads to stronger suppression, consistent with trends seen in the matter power spectrum (e.g., [95]). From the peak of $k^2 P_{\text{me}}(k)$ in Fig. 2, the density fluctuations of $k = 1\text{--}10 h \text{ Mpc}^{-1}$ contribute the most to ΔDM in Eq. (2.10).

Let us briefly summarize the current observational constraints on the T_{AGN} parameter. Chen et al. (2023) [96] detected baryon feedback suppression on the matter power spectrum

⁸These two power spectra are related via $P_{\text{me}}(k; z) = (\bar{\rho}_{\text{m}}/\bar{\rho}_{\text{gas}}(z)) P_{\text{mg}}^{\text{HMX}}(k; z) = (\Omega_{\text{m}}/\Omega_{\text{b}})[1 - (\Omega_{\text{m}}/\Omega_{\text{b}})(\bar{\rho}_{\text{star}}(z)/\bar{\rho}_{\text{m}})]^{-1} P_{\text{mg}}^{\text{HMX}}(k; z)$, where $\bar{\rho}_{\text{m}}, \bar{\rho}_{\text{gas}}$ and $\bar{\rho}_{\text{star}}$ are the mean densities of matter, gas, and stars, respectively ($\bar{\rho}_{\text{m}}$ is constant while the others are functions of z). The ratio $\bar{\rho}_{\text{star}}(z)/\bar{\rho}_{\text{m}}$ is obtained by averaging the stellar fraction (Eq. (27) in [72]) over all halo masses.

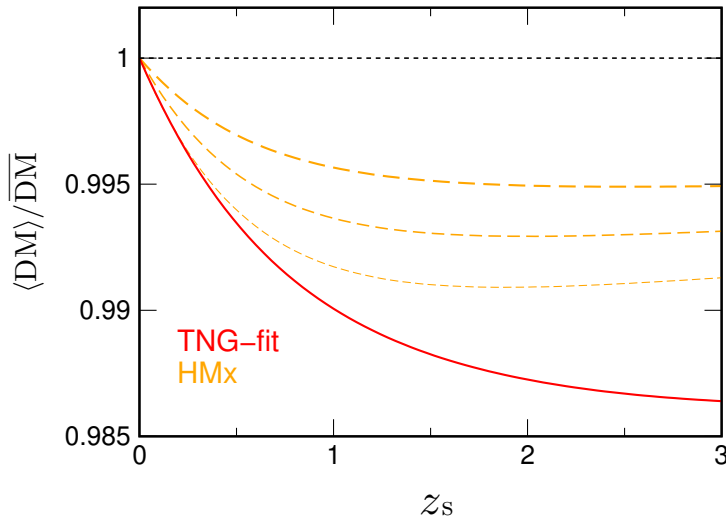


Figure 3. The ensemble average of the DM in an inhomogeneous universe $\langle \text{DM} \rangle$ normalized by that in the corresponding homogeneous model $\overline{\text{DM}}$ as a function of source redshift z_s . These curves are distinguished by the P_{me} model: the solid red curve uses the fitting function (2.12) for TNG, and the dashed orange curves use HMX with $\log_{10}(T_{\text{AGN}}/\text{K}) = 7.6$ (thin), 7.8 (average) and 8.0 (thick). The dashed curves for $z_s > 1$ are obtained from an extrapolation of HMX (which is calibrated up to $z = 1$).

using cosmic shear measurements from the Dark Energy Survey (DES) year 3 data. They found that the suppression was consistent with values of $\log_{10}(T_{\text{AGN}}/\text{K}) = 7.8$ and 8.0 (their Fig. 8), which is consistent with other cosmic shear analyses [97, 98]. On the other hand, Terasawa et al. (2024) [99] performed a similar analysis using the Subaru Hyper Suprime-Cam three-year data, probing down to very small scales (0.28 arcmin). Their findings suggest a preference for weaker feedback with $\log_{10}(T_{\text{AGN}}/\text{K}) = 7.6$ (their Fig. 11; also discussed in [100]). Tröster et al. (2022) [79] performed a combined analysis of cosmic shear from the Kilo-Degree Survey and the thermal Sunyaev–Zel’dovich data from Planck and the Atacama Cosmology Telescope. Their constraint is $\log_{10}(T_{\text{AGN}}/\text{K}) = 7.96^{+0.20}_{-0.48}$. Ferreira et al. (2024) [101] measured a cross-power spectrum of weak lensing in DES Y3 and the diffuse X-ray background in the Roentgensatellit (ROSAT), providing a very precise constraint of $\log_{10}(T_{\text{AGN}}/\text{K}) = 7.998 \pm 0.008$. In summary, the constraints do not converge well among the different measurements.

3 Results

This section presents our main results for $\langle \text{DM} \rangle$ as described in Eq. (2.9). Figure 3 illustrates $\langle \text{DM} \rangle$ normalized by $\overline{\text{DM}}$ as a function of z_s . Here, we set $f_e = 0.83$ and $X = 1 - Y = 0.76$ in Eq. (2.4), noting that the ratio $\langle \text{DM} \rangle / \overline{\text{DM}}$ is independent of f_e , X and Y as long as these quantities are constant. The TNG results exhibit a stronger lensing bias owing to weaker baryon feedback. For TNG, $\langle \text{DM} \rangle$ is 1% (0.6%) smaller than $\overline{\text{DM}}$ at $z_s = 1$ ($z_s = 0.5$), with the bias becoming more pronounced at higher z_s . For HMX, $\langle \text{DM} \rangle$ is 0.4%–0.8% smaller than $\overline{\text{DM}}$ at $z_s = 1$, depending on the value of T_{AGN} . Notably, HMX is calibrated only up to $z = 1$; thus, the results for $z_s > 1$ are extrapolated. If the baryonic feedback is ignored (i.e., $b_e = 1$), ΔDM becomes approximately twice the TNG result. In summary, the conventional

formula for $\overline{\text{DM}}$ slightly overestimates the DM owing to the gravitational lensing effect, where light rays tend to avoid dense matter clumps.

We estimate the number of localized FRBs needed to detect the lensing bias in the DM- z relation for $z_s = 0.5$ and 1. While the total DM comprises contributions from the MW, host galaxy, and cosmological sources, the lensing bias impacts the cosmological component. Referring to Fig. 3, the discrepancy between $\langle \text{DM} \rangle$ and $\overline{\text{DM}}$ is

$$\begin{aligned} \langle \text{DM} \rangle(z_s) - \overline{\text{DM}}(z_s) &\approx -3.0 \text{ pc/cm}^3 \left(\frac{\langle \text{DM} \rangle / \overline{\text{DM}}}{0.994} \right) \quad \text{for } z_s = 0.5, \\ &\approx -10 \text{ pc/cm}^3 \left(\frac{\langle \text{DM} \rangle / \overline{\text{DM}}}{0.99} \right) \quad \text{for } z_s = 1, \end{aligned} \quad (3.1)$$

for the TNG result. Here, we have used the approximate relation $\overline{\text{DM}}(z_s) \approx 1000 z_s \text{ pc/cm}^3$ (e.g., [30]). The standard deviation of the measured DM (σ_{DM}) arises from cosmological contribution ($\sigma_{\text{DM,cosmo}}$) and host-galaxy contribution ($\sigma_{\text{DM,host}}$): $\sigma_{\text{DM}} = (\sigma_{\text{DM,cosmo}}^2 + \sigma_{\text{DM,host}}^2)^{1/2}$. Using $\sigma_{\text{DM,cosmo}} \approx 200 z_s^{1/2} \text{ pc/cm}^3$ (e.g., [59, 63, 102]) and $\sigma_{\text{DM,host}} \approx 100 (1 + z_s)^{-1} \text{ pc/cm}^3$ (e.g., [25, 103, 104]), the standard deviation is

$$\begin{aligned} \sigma_{\text{DM}}(z_s) &\approx 160 \text{ pc/cm}^3 \quad \text{for } z_s = 0.5, \\ &\approx 210 \text{ pc/cm}^3 \quad \text{for } z_s = 1. \end{aligned} \quad (3.2)$$

Using many FRBs, the standard deviation decreases inversely proportional to the square root of their count. Therefore, according to Eqs. (3.1) and (3.2), when approximately 3000 and 400 localized FRBs are available for $z_s = 0.5$ and 1, respectively, the lensing bias will affect $\langle \text{DM} \rangle$ at the 1σ error level. In the near future, instruments such as the Canadian Hydrogen Intensity Mapping Experiment FRB instrument (CHIME/FRB) outriggers, the Canadian Hydrogen Observatory and Radio-transient Detector (CHORD)⁹, and the Deep Synoptic Array (DSA)-2000¹⁰ are expected to detect $\sim 10^4$ localized FRBs per year (e.g., [105–107]). With the many FRBs available, the lensing bias must be carefully considered in the DM- z relation.

There are two types of FRBs: repeaters and non-repeaters. Multiple signals from a repeater are consolidated into a single event when calculating $\langle \text{DM} \rangle$ to prevent duplication. In contrast, multiple images of a single source resulting from strong lensing are treated as independent events because their light ray paths differ. However, the probability of such lensing occurrences is relatively low, e.g., $\approx 10^{-3}$ for lensing by a galaxy and $\approx 10^{-5}$ for lensing by a galaxy cluster (e.g., [108]).

The numerical results in Fig. 3 can be fitted by a simple function:

$$\frac{\langle \text{DM} \rangle(z_s)}{\overline{\text{DM}}(z_s)} = 1 - \frac{1}{az_s^\gamma + b}, \quad (3.3)$$

where the second term corresponds to $\Delta \text{DM} / \overline{\text{DM}}$. The fitting parameters are $(a, b, \gamma) = (37, 63, -1.2)$ for TNG and $(a, b, \gamma) = (24, 136, -1.6)$ for HMX with $\log_{10}(T_{\text{AGN}}/\text{K}) = 7.8$. The relative difference between the numerical results and the fitting functions is less than 2.2×10^{-4} and 3.8×10^{-4} for TNG and HMX, respectively, over the range of $z_s = 0-3$.

⁹<https://www.chord-observatory.ca/home>

¹⁰<https://www.deepsynoptic.org/>

4 Magnification bias

Gravitational lensing in an inhomogeneous universe magnifies (or demagnifies) the flux of a source by a magnification factor μ . As a light ray traverses a higher (or lower) density region, both the DM and magnification increase (or decrease); thus, the DM correlates with magnification. Because sources fainter than the detection threshold cannot be observed, more demagnified sources are likely to be missed compared to magnified ones. Therefore, the observed sample includes brighter, magnified events with higher DMs (or excludes fainter, demagnified events with lower DMs). This observational selection bias is known as magnification bias (e.g., [65, 109, 110]). This section addresses this bias in $\langle \text{DM} \rangle$.

The observed (lensed) luminosity L_{obs} and the unlensed luminosity L are related as $L_{\text{obs}} = \mu L$. Because the number density of sources is conserved with and without lensing magnification, we have $\Phi_{\text{obs}}(L_{\text{obs}}; z_s) dL_{\text{obs}} = \Phi(L; z_s) dL$, where $\Phi_{\text{obs}}(\Phi)$ is the luminosity function with (without) lensing. The lensed luminosity function is then expressed as

$$\Phi_{\text{obs}}(L_{\text{obs}}; z_s) = \int_{\mu_{\text{min}}}^{\infty} \frac{d\mu}{\mu} P_{\mu}(\mu; z_s) \Phi\left(\frac{L_{\text{obs}}}{\mu}; z_s\right), \quad (4.1)$$

where P_{μ} is the probability distribution function of μ , satisfying $\int d\mu P_{\mu} = 1$ and $\int d\mu \mu P_{\mu} = \langle \mu \rangle = 1$. The minimum magnification μ_{min} is given as $\mu_{\text{min}} = (1 - \kappa_{\text{min}})^{-2}$ where the minimum convergence κ_{min} is obtained in Eq. (A.7) with $\delta_m = -1$ (the empty beam). The ensemble average of the DM with the magnification bias is obtained from Eq. (4.1):

$$\langle \text{DM} \rangle_{\text{mag}}(z_s) = \frac{\int_{\mu_{\text{min}}}^{\infty} d\mu \mu^{-1} \int_{L_{\text{obs,thr}}}^{\infty} dL_{\text{obs}} \int_0^{\infty} d\text{DM} P_{\mu, \text{DM}}(\mu, \text{DM}; z_s) \text{DM} \Phi(L_{\text{obs}} \mu^{-1}; z_s)}{\int_{\mu_{\text{min}}}^{\infty} d\mu \mu^{-1} \int_{L_{\text{obs,thr}}}^{\infty} dL_{\text{obs}} P_{\mu}(\mu; z_s) \Phi(L_{\text{obs}} \mu^{-1}; z_s)}, \quad (4.2)$$

where $P_{\mu, \text{DM}}$ is the joint probability distribution function of μ and the DM. If there is no correlation between them (i.e., $P_{\mu, \text{DM}}(\mu, \text{DM}) = P_{\mu}(\mu) \times P_{\text{DM}}(\text{DM})$), $\langle \text{DM} \rangle_{\text{mag}}$ reduces to $\langle \text{DM} \rangle$ in Eq. (2.9). The threshold luminosity $L_{\text{obs,thr}}$ is determined by the flux limit f_{thr} as $L_{\text{obs,thr}} = 4\pi D_L^2 f_{\text{thr}}$. To calculate $\langle \text{DM} \rangle_{\text{mag}}$, a theoretical model of $P_{\mu, \text{DM}}$ and Φ is necessary; however, $P_{\mu, \text{DM}}$ has not yet been studied extensively (cosmological ray-tracing simulations would be required to obtain $P_{\mu, \text{DM}}$). Instead, we will calculate $\langle \text{DM} \rangle_{\text{mag}}$ under a few assumptions in the following.

Considering the luminosity function of a power-law form, $\Phi \propto L^{-\alpha}$ (α is a constant), $\langle \text{DM} \rangle_{\text{mag}}$ in Eq. (4.2) reduces to a simpler form:

$$\begin{aligned} \langle \text{DM} \rangle_{\text{mag}}(z_s) &= \frac{\int_{\mu_{\text{min}}}^{\infty} d\mu \int_0^{\infty} d\text{DM} P_{\mu, \text{DM}}(\mu, \text{DM}; z_s) \mu^{\alpha-1} \text{DM}}{\int_{\mu_{\text{min}}}^{\infty} d\mu P_{\mu}(\mu; z_s) \mu^{\alpha-1}}, \\ &= \frac{\langle \mu^{\alpha-1} \text{DM} \rangle}{\langle \mu^{\alpha-1} \rangle}. \end{aligned} \quad (4.3)$$

This equation indicates that the magnification bias disappears when $\alpha = 1$. We further use the weak lensing approximation, in which the magnification can be expanded as $\mu =$

$[(1 - \kappa)^2 - \gamma^2]^{-1} \simeq 1 + 2\kappa + 3\kappa^2 + \gamma^2$ with $|\kappa|, |\gamma| \ll 1$. Using $\langle \kappa^2 \rangle = \langle \gamma^2 \rangle$ and $\langle \kappa \rangle = -2\langle \kappa^2 \rangle$, the denominator of Eq. (4.3) is

$$\langle \mu^{\alpha-1} \rangle \simeq 1 + 2(\alpha - 1)(\alpha - 2)\langle \kappa^2 \rangle.$$

Using Eqs. (2.9) and (A.6), the numerator is

$$\langle \mu^{\alpha-1} \text{DM} \rangle \simeq \overline{\text{DM}} + 2(\alpha - 1)(\alpha - 2)\langle \kappa^2 \rangle \overline{\text{DM}} + (2 - \alpha)\Delta\text{DM}.$$

Here, we have neglected the third and higher order terms of the perturbative quantities (κ , γ , and ΔDM). Finally, $\langle \text{DM} \rangle_{\text{mag}}$ simplifies to

$$\langle \text{DM} \rangle_{\text{mag}}(z_s) \simeq \overline{\text{DM}}(z_s) + \Delta\text{DM}(z_s) + (1 - \alpha)\Delta\text{DM}(z_s). \quad (4.4)$$

The second term represents the primary correction discussed in Section 2, while the third accounts for magnification bias. Both terms introduce a comparable bias (ΔDM). For larger values of α (> 1), there are more faint sub-threshold sources than super-threshold ones. Some of these sub-threshold sources become detectable owing to magnification, thereby increasing $\langle \text{DM} \rangle_{\text{mag}}$ (where $\Delta\text{DM} < 0$). For $\alpha = 2$, this increase cancels out the lensing bias in the second term of Eq. (4.4). The opposite is true for smaller values of α (< 1). Some of the many super-threshold sources are lost owing to demagnification; thus, the magnification bias decreases $\langle \text{DM} \rangle_{\text{mag}}$. A plot of $\langle \text{DM} \rangle_{\text{mag}}/\overline{\text{DM}}$ as a function of z_s is the same as in Fig. 3, but the deviation from unity is multiplied by a factor of $(2 - \alpha)$.

The index α of the FRB luminosity (or energy) function remains poorly constrained by current observations. Previous studies have predominantly explored either a single power-law function (e.g., [111, 112]) or a Schechter function¹¹ (e.g., [113–115]) to fit observational data, yielding best-fit values of α ranging broadly from 0.4 to 1.8. A more precise determination of α is needed to estimate $\langle \text{DM} \rangle_{\text{mag}}$.

5 Discussion

5.1 The other second-order effects on $\langle \text{DM} \rangle$

We have examined the lensing bias affecting $\langle \text{DM} \rangle$. However, other second-order terms in perturbation theory also affect $\langle \text{DM} \rangle$. According to previous studies concerning $\langle D_L \rangle$ (e.g., [38–40, 46]), the lensing bias dominates over other second-order effects for $z_s \gtrsim 0.3$, suggesting a similar dominance for $\langle \text{DM} \rangle$. These additional factors include the Doppler effect from the peculiar motions of the observer and source, the integrated Sachs–Wolfe (ISW) effect owing to potential evolution along the photon path, and the SW effect arising from potential differences between the observer and source. The peculiar velocity is approximately $v/c \approx 10^{-3} [v/(300 \text{ km/s})]$, and the galactic potential is $|\phi|/c^2 \approx 10^{-5} - 10^{-6}$, both of which are smaller than the lensing convergence $|\kappa| \approx \langle \kappa^2 \rangle^{1/2} \approx 10^{-2} z_s$. These effects introduce a slight bias on the source redshift of the order of $(v/c)^2$ for the peculiar velocity, $(\phi/c^2)^2$ for the potential term, and $(v\phi/c^4)$ for their cross term (e.g., [46]). The quantitative assessment of all second-order effects on $\langle \text{DM} \rangle$ is beyond the scope of this paper and remains a topic for future investigation.

¹¹A Schechter function is the same as the power-law model but incorporating an exponential cutoff at a high L .

5.2 Rotation measure

The lensing bias can also be directly applied to the cosmological rotation measure (RM) (e.g., a review [116]). When a radio signal propagates through a magnetized plasma, its polarization angle undergoes Faraday rotation (e.g., [117]). The RM is derived from the frequency-dependent rotation angle. Similar to the DM, the RM is expressed as (e.g., [118])

$$\text{RM}(z_s) = \frac{e^3}{2\pi m_e^2 c^4} \int_0^{\lambda_s} d\lambda n_e(\mathbf{r}; z) B_{\parallel}(\mathbf{r}; z) (1+z)^2, \quad (5.1)$$

where e and m_e are the electric charge and mass of the electron, respectively, and B_{\parallel} is the comoving magnetic field component along the line of sight. Because light rays propagate through underdense regions owing to lensing, we expect that the lensing bias also influences $\langle |\text{RM}| \rangle$ ¹². Estimating the lensing bias in $\langle |\text{RM}| \rangle$ requires the cross-power spectrum of matter and $n_e B_{\parallel}$ fluctuations, which is beyond the scope of this study.

6 Conclusions

We investigated the lensing effects on the ensemble average of the cosmological dispersion measure, $\langle \text{DM} \rangle$. Using the cosmological perturbation theory, we derived the primary correction term in $\langle \text{DM} \rangle$ involving the cross-power spectrum of matter and free electrons. We found that $\langle \text{DM} \rangle$ is 0.4%–1% smaller than the DM in the homogeneous cosmological model at $z_s = 1$, based on recent hydrodynamic simulations of IllustrisTNG and BAHAMAS. The impact of lensing bias becomes more pronounced for higher z_s and in scenarios with weaker baryonic feedback models. Additionally, we discussed magnification bias, where brighter magnified sources with higher DM values are preferentially included in the observed sample. The magnification bias introduces a similar level of bias, $\mathcal{O}(0.1\%–1\%)$, on $\langle \text{DM} \rangle$ depending on the luminosity (or energy) function of FRBs.

Upcoming detectors, such as the CHIME/FRB outriggers, CHORD, and DSA-2000, are expected to detect $\approx 10^4$ localized FRBs annually. During this era, it will be crucial to account for lensing bias, including magnification bias, to achieve accuracy at the percent level in the DM– z relation.

References

- [1] S. Bhandari and C. Flynn, *Probing the Universe with Fast Radio Bursts*, *Universe* **7** (2021) 85.
- [2] D. Xiao, F. Wang and Z. Dai, *The physics of fast radio bursts*, *Science China Physics, Mechanics, and Astronomy* **64** (2021) 249501 [[arXiv:2101.04907](#)].
- [3] E. Petroff, J.W.T. Hessels and D.R. Lorimer, *Fast radio bursts at the dawn of the 2020s*, *The Astronomy and Astrophysics Review* **30** (2022) 2 [[arXiv:2107.10113](#)].
- [4] B. Zhang, *The physics of fast radio bursts*, *Reviews of Modern Physics* **95** (2023) 035005 [[arXiv:2212.03972](#)].
- [5] E.F. Keane, S. Johnston, S. Bhandari, E. Barr, N.D.R. Bhat, M. Burgay et al., *The host galaxy of a fast radio burst*, *nature* **530** (2016) 453 [[arXiv:1602.07477](#)].
- [6] S. Chatterjee, C.J. Law, R.S. Wharton, S. Burke-Spolaor, J.W.T. Hessels, G.C. Bower et al., *A direct localization of a fast radio burst and its host*, *nature* **541** (2017) 58 [[arXiv:1701.01098](#)].

¹²Here, $\langle \text{RM} \rangle = 0$ because $\langle B_{\parallel} \rangle = 0$.

- [7] S. Bhandari, K.E. Heintz, K. Aggarwal, L. Marnoch, C.K. Day, J. Sydnor et al., *Characterizing the Fast Radio Burst Host Galaxy Population and its Connection to Transients in the Local and Extragalactic Universe*, *The Astronomical Journal* **163** (2022) 69 [[arXiv:2108.01282](#)].
- [8] M. Bhardwaj, D. Michilli, A.Y. Kirichenko, O. Modilim, K. Shin, V.M. Kaspi et al., *Host Galaxies for Four Nearby CHIME/FRB Sources and the Local Universe FRB Host Galaxy Population*, *arXiv e-prints* (2023) [arXiv:2310.10018](#).
- [9] A.C. Gordon, W.-f. Fong, C.D. Kilpatrick, T. Eftekhari, J. Leja, J.X. Prochaska et al., *The Demographics, Stellar Populations, and Star Formation Histories of Fast Radio Burst Host Galaxies: Implications for the Progenitors*, *Astrophys. J.* **954** (2023) 80 [[arXiv:2302.05465](#)].
- [10] A.L. Ibik, M.R. Drout, B.M. Gaensler, P. Scholz, D. Michilli, M. Bhardwaj et al., *Proposed Host Galaxies of Repeating Fast Radio Burst Sources Detected by CHIME/FRB*, *Astrophys. J.* **961** (2024) 99 [[arXiv:2304.02638](#)].
- [11] C.J. Law, K. Sharma, V. Ravi, G. Chen, M. Catha, L. Connor et al., *Deep Synoptic Array Science: First FRB and Host Galaxy Catalog*, *Astrophys. J.* **967** (2024) 29 [[arXiv:2307.03344](#)].
- [12] S.D. Ryder, K.W. Bannister, S. Bhandari, A.T. Deller, R.D. Ekers, M. Glowacki et al., *A luminous fast radio burst that probes the Universe at redshift 1*, *Science* **382** (2023) 294 [[arXiv:2210.04680](#)].
- [13] Z. Li, H. Gao, J.J. Wei, Y.P. Yang, B. Zhang and Z.H. Zhu, *Cosmology-insensitive estimate of IGM baryon mass fraction from five localized fast radio bursts*, *Mon. Not. Roy. Astron. Soc.* **496** (2020) L28 [[arXiv:2004.08393](#)].
- [14] T. Lemos, R. Gonçalves, J. Carvalho and J. Alcaniz, *Forecasting constraints on the baryon mass fraction in the IGM from fast radio bursts and type Ia supernovae*, *European Physical Journal C* **83** (2023) 1128 [[arXiv:2307.06911](#)].
- [15] H.-N. Lin and R. Zou, *Probing the baryon mass fraction in IGM and its redshift evolution with fast radio bursts using Bayesian inference method*, *Mon. Not. Roy. Astron. Soc.* **520** (2023) 6237 [[arXiv:2302.10585](#)].
- [16] B. Wang and J.-J. Wei, *An 8.0% Determination of the Baryon Fraction in the Intergalactic Medium from Localized Fast Radio Bursts*, *Astrophys. J.* **944** (2023) 50 [[arXiv:2211.02209](#)].
- [17] I.S. Khrykin, M. Ata, K.-G. Lee, S. Simha, Y. Huang, J.X. Prochaska et al., *FLIMFLAM DR1: The First Constraints on the Cosmic Baryon Distribution from 8 FRB sightlines*, *arXiv e-prints* (2024) [arXiv:2402.00505](#).
- [18] S. Hagstotz, R. Reischke and R. Lilow, *A new measurement of the Hubble constant using fast radio bursts*, *Mon. Not. Roy. Astron. Soc.* **511** (2022) 662 [[arXiv:2104.04538](#)].
- [19] C.W. James, E.M. Ghosh, J.X. Prochaska, K.W. Bannister, S. Bhandari, C.K. Day et al., *A measurement of Hubble's Constant using Fast Radio Bursts*, *Mon. Not. Roy. Astron. Soc.* **516** (2022) 4862 [[arXiv:2208.00819](#)].
- [20] Q. Wu, G.-Q. Zhang and F.-Y. Wang, *An 8 per cent determination of the Hubble constant from localized fast radio bursts*, *Mon. Not. Roy. Astron. Soc.* **515** (2022) L1 [[arXiv:2108.00581](#)].
- [21] J.A.S. Fortunato, W.S. Hipólito-Ricaldi and M.V. dos Santos, *Cosmography from well-localized fast radio bursts*, *Mon. Not. Roy. Astron. Soc.* **526** (2023) 1773 [[arXiv:2307.04711](#)].
- [22] Y. Liu, H. Yu and P. Wu, *Cosmological-model-independent Determination of Hubble Constant from Fast Radio Bursts and Hubble Parameter Measurements*, *Astrophys. J. Lett.* **946** (2023) L49 [[arXiv:2210.05202](#)].

- [23] J.-J. Wei and F. Melia, *Investigating Cosmological Models and the Hubble Tension Using Localized Fast Radio Bursts*, *Astrophys. J.* **955** (2023) 101 [[arXiv:2308.05918](#)].
- [24] J. Gao, Z. Zhou, M. Du, R. Zou, J. Hu and L. Xu, *A measurement of Hubble constant using cosmographic approach combining fast radio bursts and supernovae*, *Mon. Not. Roy. Astron. Soc.* **527** (2024) 7861 [[arXiv:2307.08285](#)].
- [25] J.P. Macquart, J.X. Prochaska, M. McQuinn, K.W. Bannister, S. Bhandari, C.K. Day et al., *A census of baryons in the Universe from localized fast radio bursts*, *nature* **581** (2020) 391 [[arXiv:2005.13161](#)].
- [26] K.B. Yang, Q. Wu and F.Y. Wang, *Finding the Missing Baryons in the Intergalactic Medium with Localized Fast Radio Bursts*, *Astrophys. J. Lett.* **940** (2022) L29 [[arXiv:2211.04058](#)].
- [27] H. Gao, Z. Li and B. Zhang, *Fast Radio Burst/Gamma-Ray Burst Cosmography*, *Astrophys. J.* **788** (2014) 189 [[arXiv:1402.2498](#)].
- [28] B. Zhou, X. Li, T. Wang, Y.-Z. Fan and D.-M. Wei, *Fast radio bursts as a cosmic probe?*, *Phys. Rev. D.* **89** (2014) 107303 [[arXiv:1401.2927](#)].
- [29] A. Walters, A. Weltman, B.M. Gaensler, Y.-Z. Ma and A. Witzemann, *Future Cosmological Constraints From Fast Radio Bursts*, *Astrophys. J.* **856** (2018) 65 [[arXiv:1711.11277](#)].
- [30] K. Ioka, *The Cosmic Dispersion Measure from Gamma-Ray Burst Afterglows: Probing the Reionization History and the Burst Environment*, *Astrophys. J. Lett.* **598** (2003) L79 [[astro-ph/0309200](#)].
- [31] S. Inoue, *Probing the cosmic reionization history and local environment of gamma-ray bursts through radio dispersion*, *Mon. Not. Roy. Astron. Soc.* **348** (2004) 999 [[astro-ph/0309364](#)].
- [32] Z. Zheng, E.O. Ofek, S.R. Kulkarni, J.D. Neill and M. Juric, *Probing the Intergalactic Medium with Fast Radio Bursts*, *Astrophys. J.* **797** (2014) 71 [[arXiv:1409.3244](#)].
- [33] M. Caleb, C. Flynn and B.W. Stappers, *Constraining the era of helium reionization using fast radio bursts*, *Mon. Not. Roy. Astron. Soc.* **485** (2019) 2281 [[arXiv:1902.06981](#)].
- [34] P. Beniamini, P. Kumar, X. Ma and E. Quataert, *Exploring the epoch of hydrogen reionization using FRBs*, *Mon. Not. Roy. Astron. Soc.* **502** (2021) 5134 [[arXiv:2011.11643](#)].
- [35] T. Hashimoto, T. Goto, T.-Y. Lu, A.Y.L. On, D.J.D. Santos, S.J. Kim et al., *Revealing the cosmic reionization history with fast radio bursts in the era of Square Kilometre Array*, *Mon. Not. Roy. Astron. Soc.* **502** (2021) 2346 [[arXiv:2101.08798](#)].
- [36] J. Adamek, C. Clarkson, L. Coates, R. Durrer and M. Kunz, *Bias and scatter in the Hubble diagram from cosmological large-scale structure*, *Phys. Rev. D.* **100** (2019) 021301 [[arXiv:1812.04336](#)].
- [37] E. Barausse, S. Matarrese and A. Riotto, *Effect of inhomogeneities on the luminosity distance-redshift relation: Is dark energy necessary in a perturbed universe?*, *Phys. Rev. D.* **71** (2005) 063537 [[astro-ph/0501152](#)].
- [38] I. Ben-Dayan, G. Marozzi, F. Nugier and G. Veneziano, *The second-order luminosity-redshift relation in a generic inhomogeneous cosmology*, *JCAP* **2012** (2012) 045 [[arXiv:1209.4326](#)].
- [39] I. Ben-Dayan, M. Gasperini, G. Marozzi, F. Nugier and G. Veneziano, *Average and dispersion of the luminosity-redshift relation in the concordance model*, *JCAP* **2013** (2013) 002 [[arXiv:1302.0740](#)].
- [40] I. Ben-Dayan, M. Gasperini, G. Marozzi, F. Nugier and G. Veneziano, *Do Stochastic Inhomogeneities Affect Dark-Energy Precision Measurements?*, *Phys. Rev. Lett.* **110** (2013) 021301 [[arXiv:1207.1286](#)].

- [41] C. Bonvin, C. Clarkson, R. Durrer, R. Maartens and O. Umeh, *Do we care about the distance to the CMB? Clarifying the impact of second-order lensing*, *JCAP* **2015** (2015) 050 [[arXiv:1503.07831](#)].
- [42] M.-A. Breton and P. Fleury, *Theoretical and numerical perspectives on cosmic distance averages*, *Astron. Astrophys.* **655** (2021) A54 [[arXiv:2012.07802](#)].
- [43] P. Fleury, C. Clarkson and R. Maartens, *How does the cosmic large-scale structure bias the Hubble diagram?*, *JCAP* **2017** (2017) 062 [[arXiv:1612.03726](#)].
- [44] N. Kaiser and J.A. Peacock, *On the bias of the distance-redshift relation from gravitational lensing*, *Mon. Not. Roy. Astron. Soc.* **455** (2016) 4518 [[arXiv:1503.08506](#)].
- [45] G. Marozzi, *The luminosity distance-redshift relation up to second order in the Poisson gauge with anisotropic stress*, *Classical and Quantum Gravity* **32** (2015) 045004 [[arXiv:1406.1135](#)].
- [46] O. Umeh, C. Clarkson and R. Maartens, *Nonlinear relativistic corrections to cosmological distances, redshift and gravitational lensing magnification: I. Key results*, *Classical and Quantum Gravity* **31** (2014) 202001 [[arXiv:1207.2109](#)].
- [47] O. Umeh, C. Clarkson and R. Maartens, *Nonlinear relativistic corrections to cosmological distances, redshift and gravitational lensing magnification: II. Derivation*, *Classical and Quantum Gravity* **31** (2014) 205001 [[arXiv:1402.1933](#)].
- [48] P. Helbig, *Calculation of distances in cosmological models with small-scale inhomogeneities and their use in observational cosmology: a review*, *The Open Journal of Astrophysics* **3** (2020) 1 [[arXiv:1912.12269](#)].
- [49] C. Clarkson, O. Umeh, R. Maartens and R. Durrer, *What is the distance to the CMB?*, *JCAP* **2014** (2014) 036 [[arXiv:1405.7860](#)].
- [50] D.E. Holz and E.V. Linder, *Safety in Numbers: Gravitational Lensing Degradation of the Luminosity Distance-Redshift Relation*, *Astrophys. J.* **631** (2005) 678 [[astro-ph/0412173](#)].
- [51] J. Jönsson, M. Sullivan, I. Hook, S. Basa, R. Carlberg, A. Conley et al., *Constraining dark matter halo properties using lensed Supernova Legacy Survey supernovae*, *Mon. Not. Roy. Astron. Soc.* **405** (2010) 535 [[arXiv:1002.1374](#)].
- [52] P. Shah, P. Lemos and O. Lahav, *Weak-lensing magnification of Type Ia supernovae from the Pantheon sample*, *Mon. Not. Roy. Astron. Soc.* **515** (2022) 2305 [[arXiv:2203.09865](#)].
- [53] P. Shah, T.M. Davis, D. Bacon, D. Brout, J. Frieman, L. Galbany et al., *The Dark Energy Survey : Detection of weak lensing magnification of supernovae and constraints on dark matter haloes*, *Mon. Not. Roy. Astron. Soc.* (2024) [[arXiv:2406.05047](#)].
- [54] P. Shah, P. Lemos and O. Lahav, *The impact of weak lensing on Type Ia supernovae luminosity distances*, *Mon. Not. Roy. Astron. Soc.* **520** (2023) L68 [[arXiv:2210.10688](#)].
- [55] S. Weinberg, *Apparent luminosities in a locally inhomogeneous universe.*, *Astrophys. J. Lett.* **208** (1976) L1.
- [56] R. Takahashi, M. Oguri, M. Sato and T. Hamana, *Probability Distribution Functions of Cosmological Lensing: Convergence, Shear, and Magnification*, *Astrophys. J.* **742** (2011) 15 [[arXiv:1106.3823](#)].
- [57] M. Mizuno and T. Suyama, *Weak lensing of gravitational waves in wave optics: Beyond the Born approximation*, *Phys. Rev. D.* **108** (2023) 043511 [[arXiv:2210.02062](#)].
- [58] M. Mizuno, T. Suyama and R. Takahashi, *New consistency relations between averages and variances of weakly lensed signals of gravitational waves*, *Phys. Rev. D.* **109** (2024) 083505 [[arXiv:2309.04114](#)].
- [59] M. McQuinn, *Locating the “Missing” Baryons with Extragalactic Dispersion Measure Estimates*, *Astrophys. J. Lett.* **780** (2014) L33 [[arXiv:1309.4451](#)].

- [60] K. Dolag, B.M. Gaensler, A.M. Beck and M.C. Beck, *Constraints on the distribution and energetics of fast radio bursts using cosmological hydrodynamic simulations*, *Mon. Not. Roy. Astron. Soc.* **451** (2015) 4277 [[arXiv:1412.4829](#)].
- [61] M. Shirasaki, K. Kashiyama and N. Yoshida, *Large-scale clustering as a probe of the origin and the host environment of fast radio bursts*, *Phys. Rev. D.* **95** (2017) 083012 [[arXiv:1702.07085](#)].
- [62] M. Jaroszynski, *Fast radio bursts and cosmological tests*, *Mon. Not. Roy. Astron. Soc.* **484** (2019) 1637 [[arXiv:1812.11936](#)].
- [63] R. Takahashi, K. Ioka, A. Mori and K. Funahashi, *Statistical modelling of the cosmological dispersion measure*, *Mon. Not. Roy. Astron. Soc.* **502** (2021) 2615 [[arXiv:2010.01560](#)].
- [64] Planck Collaboration, *Planck 2015 results. XIII. Cosmological parameters*, *Astron. Astrophys.* **594** (2016) A13 [[arXiv:1502.01589](#)].
- [65] M. Bartelmann and P. Schneider, *Weak gravitational lensing*, *Phys. Rep.* **340** (2001) 291 [[astro-ph/9912508](#)].
- [66] S. Dodelson and F. Schmidt, *Modern Cosmology* (2020), [10.1016/C2017-0-01943-2](#).
- [67] X. Er and S. Mao, *Effects of plasma on gravitational lensing*, *Mon. Not. Roy. Astron. Soc.* **437** (2014) 2180 [[arXiv:1310.5825](#)].
- [68] F.T. Haddock and D.W. Sciama, *Proposal for the Detection of Dispersion in Radio-Wave Propagation Through Intergalactic Space*, *Phys. Rev. Lett.* **14** (1965) 1007.
- [69] V.L. Ginzburg, *Possibility of Determining Intergalactic Gas Density by Radio Observations of Flares of Remote Sources*, *nature* **246** (1973) 415.
- [70] D.M. Palmer, *Radio Dispersion as a Diagnostic of Gamma-Ray Burst Distances*, *Astrophys. J. Lett.* **417** (1993) L25.
- [71] W. Deng and B. Zhang, *Cosmological Implications of Fast Radio Burst/Gamma-Ray Burst Associations*, *Astrophys. J. Lett.* **783** (2014) L35 [[arXiv:1401.0059](#)].
- [72] A.J. Mead, T. Tröster, C. Heymans, L. Van Waerbeke and I.G. McCarthy, *A hydrodynamical halo model for weak-lensing cross correlations*, *Astron. Astrophys.* **641** (2020) A130 [[arXiv:2005.00009](#)].
- [73] F. Marinacci, M. Vogelsberger, R. Pakmor, P. Torrey, V. Springel, L. Hernquist et al., *First results from the IllustrisTNG simulations: radio haloes and magnetic fields*, *Mon. Not. Roy. Astron. Soc.* **480** (2018) 5113 [[arXiv:1707.03396](#)].
- [74] J.P. Naiman, A. Pillepich, V. Springel, E. Ramirez-Ruiz, P. Torrey, M. Vogelsberger et al., *First results from the IllustrisTNG simulations: a tale of two elements - chemical evolution of magnesium and europium*, *Mon. Not. Roy. Astron. Soc.* **477** (2018) 1206 [[arXiv:1707.03401](#)].
- [75] D. Nelson, A. Pillepich, V. Springel, R. Weinberger, L. Hernquist, R. Pakmor et al., *First results from the IllustrisTNG simulations: the galaxy colour bimodality*, *Mon. Not. Roy. Astron. Soc.* **475** (2018) 624 [[arXiv:1707.03395](#)].
- [76] A. Pillepich, D. Nelson, L. Hernquist, V. Springel, R. Pakmor, P. Torrey et al., *First results from the IllustrisTNG simulations: the stellar mass content of groups and clusters of galaxies*, *Mon. Not. Roy. Astron. Soc.* **475** (2018) 648 [[arXiv:1707.03406](#)].
- [77] V. Springel, R. Pakmor, A. Pillepich, R. Weinberger, D. Nelson, L. Hernquist et al., *First results from the IllustrisTNG simulations: matter and galaxy clustering*, *Mon. Not. Roy. Astron. Soc.* **475** (2018) 676 [[arXiv:1707.03397](#)].
- [78] D. Nelson, V. Springel, A. Pillepich, V. Rodriguez-Gomez, P. Torrey, S. Genel et al., *The IllustrisTNG simulations: public data release*, *Computational Astrophysics and Cosmology* **6** (2019) 2 [[arXiv:1812.05609](#)].

- [79] T. Tröster, A.J. Mead, C. Heymans, Z. Yan, D. Alonso, M. Asgari et al., *Joint constraints on cosmology and the impact of baryon feedback: Combining KiDS-1000 lensing with the thermal Sunyaev-Zeldovich effect from Planck and ACT*, *Astron. Astrophys.* **660** (2022) A27 [[arXiv:2109.04458](#)].
- [80] I.G. McCarthy, J. Schaye, S. Bird and A.M.C. Le Brun, *The BAHAMAS project: calibrated hydrodynamical simulations for large-scale structure cosmology*, *Mon. Not. Roy. Astron. Soc.* **465** (2017) 2936 [[arXiv:1603.02702](#)].
- [81] I.G. McCarthy, S. Bird, J. Schaye, J. Harnois-Deraps, A.S. Font and L. van Waerbeke, *The BAHAMAS project: the CMB-large-scale structure tension and the roles of massive neutrinos and galaxy formation*, *Mon. Not. Roy. Astron. Soc.* **476** (2018) 2999 [[arXiv:1712.02411](#)].
- [82] V. Springel, *E pur si muove: Galilean-invariant cosmological hydrodynamical simulations on a moving mesh*, *Mon. Not. Roy. Astron. Soc.* **401** (2010) 791 [[arXiv:0901.4107](#)].
- [83] R.W. Hockney and J.W. Eastwood, *Computer Simulation Using Particles* (New York: McGraw-Hill) (1981).
- [84] Y.P. Jing, *Correcting for the Alias Effect When Measuring the Power Spectrum Using a Fast Fourier Transform*, *Astrophys. J.* **620** (2005) 559 [[astro-ph/0409240](#)].
- [85] E. Sefusatti, M. Crocce, R. Scoccimarro and H.M.P. Couchman, *Accurate estimators of correlation functions in Fourier space*, *Mon. Not. Roy. Astron. Soc.* (2016) [[arXiv:1512.07295](#)].
- [86] V. Springel, *The cosmological simulation code GADGET-2*, *Mon. Not. Roy. Astron. Soc.* **364** (2005) 1105 [[astro-ph/0505010](#)].
- [87] A. Cooray and R. Sheth, *Halo models of large scale structure*, *Phys. Rep.* **372** (2002) 1 [[astro-ph/0206508](#)].
- [88] G. Aricò, R.E. Angulo, C. Hernández-Monteagudo, S. Contreras, M. Zennaro, M. Pellejero-Ibañez et al., *Modelling the large-scale mass density field of the universe as a function of cosmology and baryonic physics*, *Mon. Not. Roy. Astron. Soc.* **495** (2020) 4800 [[arXiv:1911.08471](#)].
- [89] M. Shirasaki, R. Takahashi, K. Osato and K. Ioka, *Probing cosmology and gas physics with fast radio bursts: cross-correlations of dark matter haloes and cosmic dispersion measures*, *Mon. Not. Roy. Astron. Soc.* **512** (2022) 1730 [[arXiv:2108.12205](#)].
- [90] M. Asgari, A.J. Mead and C. Heymans, *The halo model for cosmology: a pedagogical review*, *The Open Journal of Astrophysics* **6** (2023) 39 [[arXiv:2303.08752](#)].
- [91] R. Reischke and S. Hagstotz, *Cosmological covariance of fast radio burst dispersions*, *Mon. Not. Roy. Astron. Soc.* **524** (2023) 2237 [[arXiv:2301.03527](#)].
- [92] R. Reischke, D. Neumann, K.A. Bertmann, S. Hagstotz and H. Hildebrandt, *Calibrating baryonic feedback with weak lensing and fast radio bursts*, *arXiv e-prints* (2023) [[arXiv:2309.09766](#)].
- [93] R.E. Smith, J.A. Peacock, A. Jenkins, S.D.M. White, C.S. Frenk, F.R. Pearce et al., *Stable clustering, the halo model and non-linear cosmological power spectra*, *Mon. Not. Roy. Astron. Soc.* **341** (2003) 1311 [[astro-ph/0207664](#)].
- [94] R. Takahashi, M. Sato, T. Nishimichi, A. Taruya and M. Oguri, *Revising the Halofit Model for the Nonlinear Matter Power Spectrum*, *Astrophys. J.* **761** (2012) 152 [[arXiv:1208.2701](#)].
- [95] N.E. Chisari, A.J. Mead, S. Joudaki, P.G. Ferreira, A. Schneider, J. Mohr et al., *Modelling baryonic feedback for survey cosmology*, *The Open Journal of Astrophysics* **2** (2019) 4 [[arXiv:1905.06082](#)].

- [96] A. Chen, G. Aricò, D. Huterer, R.E. Angulo, N. Weaverdyck, O. Friedrich et al., *Constraining the baryonic feedback with cosmic shear using the DES Year-3 small-scale measurements*, *Mon. Not. Roy. Astron. Soc.* **518** (2023) 5340 [[arXiv:2206.08591](#)].
- [97] G. Aricò, R.E. Angulo, M. Zennaro, S. Contreras, A. Chen and C. Hernández-Monteagudo, *DES Y3 cosmic shear down to small scales: Constraints on cosmology and baryons*, *Astron. Astrophys.* **678** (2023) A109 [[arXiv:2303.05537](#)].
- [98] J. Xu, T. Eifler, V. Miranda, X. Fang, E. Saraivanov, E. Krause et al., *Constraining Baryonic Physics with DES Y1 and Planck data – Combining Galaxy Clustering, Weak Lensing, and CMB Lensing*, *arXiv e-prints* (2023) arXiv:2311.08047 [[arXiv:2311.08047](#)].
- [99] R. Terasawa, X. Li, M. Takada, T. Nishimichi, S. Tanaka, S. Sugiyama et al., *Exploring the baryonic effect signature in the Hyper Suprime-Cam Year 3 cosmic shear two-point correlations on small scales: the S_8 tension remains present*, *arXiv e-prints* (2024) arXiv:2403.20323 [[2403.20323](#)].
- [100] C. García-García, M. Zennaro, G. Aricò, D. Alonso and R.E. Angulo, *Cosmic shear with small scales: DES-Y3, KiDS-1000 and HSC-DR1*, *arXiv e-prints* (2024) arXiv:2403.13794 [[2403.13794](#)].
- [101] T. Ferreira, D. Alonso, C. Garcia-Garcia and N.E. Chisari, *X-Ray-Cosmic-Shear Cross-Correlations: First Detection and Constraints on Baryonic Effects*, *Phys. Rev. Lett.* **133** (2024) 051001 [[arXiv:2309.11129](#)].
- [102] P. Kumar and E.V. Linder, *Use of fast radio burst dispersion measures as distance measures*, *Phys. Rev. D.* **100** (2019) 083533 [[arXiv:1903.08175](#)].
- [103] J.-F. Mo, W. Zhu, Y. Wang, L. Tang and L.-L. Feng, *The dispersion measure of Fast Radio Bursts host galaxies: estimation from cosmological simulations*, *Mon. Not. Roy. Astron. Soc.* **518** (2023) 539 [[arXiv:2210.14052](#)].
- [104] A. Theis, S. Hagstotz, R. Reischke and J. Weller, *Galaxy dispersion measured by Fast Radio Bursts as a probe of baryonic feedback models*, *arXiv e-prints* (2024) arXiv:2403.08611.
- [105] K. Vanderlinde, A. Liu, B. Gaensler, D. Bond, G. Hinshaw, C. Ng et al., *The Canadian Hydrogen Observatory and Radio-transient Detector (CHORD)*, in *Canadian Long Range Plan for Astronomy and Astrophysics White Papers*, vol. 2020, p. 28, 2019, DOI [[arXiv:1911.01777](#)].
- [106] C. Leung, J. Mena-Parra, K. Masui, K. Bandura, M. Bhardwaj, P.J. Boyle et al., *A Synoptic VLBI Technique for Localizing Nonrepeating Fast Radio Bursts with CHIME/FRB*, *The Astronomical Journal* **161** (2021) 81 [[arXiv:2008.11738](#)].
- [107] A.E. Lanman, S. Andrew, M. Lazda, V. Shah, M. Amiri, A. Balasubramanian et al., *CHIME/FRB Outriggers: KKO Station System and Commissioning Results*, *arXiv e-prints* (2024) arXiv:2402.07898.
- [108] M. Oguri, *Strong gravitational lensing of explosive transients*, *Reports on Progress in Physics* **82** (2019) 126901 [[arXiv:1907.06830](#)].
- [109] E.L. Turner, J.P. Ostriker and I. Gott, J. R., *The statistics of gravitational lenses : the distributions of image angular separations and lens redshifts.*, *Astrophys. J.* **284** (1984) 1.
- [110] P. Schneider, J. Ehlers and E.E. Falco, *Gravitational Lenses* (1992), [10.1007/978-3-662-03758-4](#).
- [111] T. Hashimoto, T. Goto, A.Y.L. On, T.-Y. Lu, D.J.D. Santos, S.C.C. Ho et al., *No redshift evolution of non-repeating fast radio burst rates*, *Mon. Not. Roy. Astron. Soc.* **498** (2020) 3927 [[arXiv:2008.09621](#)].

- [112] C.W. James, J.X. Prochaska, J.P. Macquart, F.O. North-Hickey, K.W. Bannister and A. Dunning, *The z -DM distribution of fast radio bursts*, *Mon. Not. Roy. Astron. Soc.* **509** (2022) 4775 [arXiv:2101.08005].
- [113] R. Luo, Y. Men, K. Lee, W. Wang, D.R. Lorimer and B. Zhang, *On the FRB luminosity function - - II. Event rate density*, *Mon. Not. Roy. Astron. Soc.* **494** (2020) 665 [arXiv:2003.04848].
- [114] T. Hashimoto, T. Goto, B.H. Chen, S.C.C. Ho, T.Y.Y. Hsiao, Y.H.V. Wong et al., *Energy functions of fast radio bursts derived from the first CHIME/FRB catalogue*, *Mon. Not. Roy. Astron. Soc.* **511** (2022) 1961 [arXiv:2201.03574].
- [115] K. Shin, K.W. Masui, M. Bhardwaj, T. Cassanelli, P. Chawla, M. Dobbs et al., *Inferring the Energy and Distance Distributions of Fast Radio Bursts Using the First CHIME/FRB Catalog*, *Astrophys. J.* **944** (2023) 105 [arXiv:2207.14316].
- [116] J.L. Han, *Observing Interstellar and Intergalactic Magnetic Fields*, *Annual Review of Astronomy and Astrophysics* **55** (2017) 111.
- [117] J. Binney and M. Merrifield, *Galactic Astronomy* (1998).
- [118] T. Akahori and D. Ryu, *Faraday Rotation Measure due to the Intergalactic Magnetic Field. II. The Cosmological Contribution*, *Astrophys. J.* **738** (2011) 134 [arXiv:1107.0142].
- [119] C. Bonvin, C. Clarkson, R. Durrer, R. Maartens and O. Umeh, *Cosmological ensemble and directional averages of observables*, *JCAP* **2015** (2015) 040 [arXiv:1504.01676].

A Derivation of the DM correction terms

This appendix provides a detailed calculation of the DM correction terms in Eq. (2.8). The second and third terms of Eq. (2.8) are written as $\Delta\text{DM}_{2\text{nd}}(z_s)$ and $\Delta\text{DM}_{3\text{rd}}(z_s)$, respectively. Substituting \mathbf{x} in Eq. (2.1) into Eq. (2.8), the second term becomes

$$\begin{aligned} \Delta\text{DM}_{2\text{nd}}(z_s) &= \frac{2}{c^2} \int_0^{r_s} dr \bar{n}_e(z) (1+z) \left[-\int_0^r dr' (r-r') + \frac{r}{r_s} \int_0^{r_s} dr' (r_s-r') \right] \\ &\quad \times \langle \nabla_{\mathbf{x}'} \phi(\mathbf{r}'; z') \cdot \nabla_{\mathbf{x}} \delta_e(\mathbf{r}; z) \rangle \Big|_{\mathbf{x}=\mathbf{x}'=0}. \end{aligned} \quad (\text{A.1})$$

Here, the integration is performed along the r -axis, and λ, λ' and λ_s have been substituted with r, r' and r_s , respectively.

The Fourier transforms of ϕ and δ_e are

$$\phi(\mathbf{r}; z) = \int \frac{d^3k}{(2\pi)^3} \tilde{\phi}(\mathbf{k}; z) e^{i\mathbf{k}\cdot\mathbf{r}}, \quad \delta_e(\mathbf{r}; z) = \int \frac{d^3k}{(2\pi)^3} \tilde{\delta}_e(\mathbf{k}; z) e^{i\mathbf{k}\cdot\mathbf{r}}. \quad (\text{A.2})$$

The gravitational potential ϕ is determined by the matter density fluctuations δ_m through the Poisson equation in Fourier space: $-k^2 \tilde{\phi}(\mathbf{k}; z) = (3/2)H_0^2 \Omega_m (1+z) \tilde{\delta}_m(\mathbf{k}; z)$. The cross correlation of $\nabla_{\mathbf{x}} \phi$ and $\nabla_{\mathbf{x}} \delta_e$ in Eq. (A.1) is rewritten using the Fourier transforms (A.2):

$$\begin{aligned} \langle \nabla_{\mathbf{x}'} \phi(\mathbf{r}'; z') \cdot \nabla_{\mathbf{x}} \delta_e(\mathbf{r}; z) \rangle \Big|_{\mathbf{x}=\mathbf{x}'=0} &= -\frac{3H_0^2 \Omega_m}{2} (1+z) \int \frac{d^3k}{(2\pi)^3} \int \frac{d^3k'}{(2\pi)^3} \frac{\mathbf{k}_{\perp} \cdot \mathbf{k}'_{\perp}}{k'^2} \\ &\quad \times \langle \tilde{\delta}_m(\mathbf{k}'; z') \tilde{\delta}_e^*(\mathbf{k}; z) \rangle e^{i(k'_{\parallel} r' - k_{\parallel} r)}, \end{aligned} \quad (\text{A.3})$$

where k_{\parallel} and \mathbf{k}_{\perp} are the wave vectors parallel and perpendicular to the r -axis (i.e., $\mathbf{k} \cdot \mathbf{r} = k_{\parallel} r + \mathbf{k}_{\perp} \cdot \mathbf{x}$), respectively. The cross-power spectrum between δ_m and δ_e is defined as

$$\langle \tilde{\delta}_m(\mathbf{k}'; z') \tilde{\delta}_e^*(\mathbf{k}; z) \rangle \equiv (2\pi)^3 \delta_D(\mathbf{k} - \mathbf{k}') P_{\text{me}}(k; z, z'), \quad (\text{A.4})$$

where δ_D is the Dirac delta function. Using Eq. (A.4), Eq. (A.3) reduces to

$$\begin{aligned} \langle \nabla_{\mathbf{x}'} \phi(\mathbf{r}'; z') \cdot \nabla_{\mathbf{x}} \delta_e(\mathbf{r}; z) \rangle \Big|_{\mathbf{x}=\mathbf{x}'=0} &= -\frac{3H_0^2 \Omega_m}{2} (1+z) \int \frac{d^3 k}{(2\pi)^3} \frac{k_\perp^2}{k^2} P_{\text{me}}(k; z, z') e^{ik_\parallel(r'-r)}, \\ &= -\frac{3H_0^2 \Omega_m}{2} (1+z) \int \frac{d^2 k_\perp}{(2\pi)^2} P_{\text{me}}(k_\perp; z) \delta_D(r'-r). \end{aligned} \quad (\text{A.5})$$

In the second equality, we applied the Limber approximation: $\int dk_\parallel e^{ik_\parallel(r'-r)} P_{\text{me}}(k; z, z') = 2\pi \delta_D(r'-r) P_{\text{me}}(k_\perp; z)$, which neglects the cross-correlation of $\phi(\mathbf{r}'; z')$ and $\delta_e(\mathbf{r}; z)$ for the different redshifts $z' \neq z$. Substituting Eq. (A.5) into Eq. (A.1) yields the following:

$$\begin{aligned} \Delta \text{DM}_{2\text{nd}}(z_s) &= -\frac{3H_0^2 \Omega_m}{2\pi c^2} \int_0^{r_s} dr \bar{n}_e(z) (1+z)^2 \frac{r(r_s-r)}{r_s} \int_0^\infty dk_\perp k_\perp P_{\text{me}}(k_\perp; z), \\ &= -2 \langle \kappa (\text{DM} - \overline{\text{DM}}) \rangle. \end{aligned} \quad (\text{A.6})$$

Here, the convergence field for the source redshift z_s is defined as

$$\kappa(z_s) = \frac{3H_0^2 \Omega_m}{2c^2} \int_0^{r_s} dr (1+z) \frac{r(r_s-r)}{r_s} \delta_m(\mathbf{r}; z). \quad (\text{A.7})$$

Therefore, the correction term $\Delta \text{DM}_{2\text{nd}}$ arises from a cross-correlation between κ and the DM. Equation (A.6) is consistent with the previous work (Section 2 of Ref. [119]) by replacing their f with the DM. Equations (A.6) and (2.9) agree with the previous result for the convergence [44, 56], $\langle \kappa \rangle = -2 \langle \kappa^2 \rangle$, by replacing $\bar{n}_e \delta_e$ with $(3H_0^2 \Omega_m / 2c^2) [r(r_s-r)/r_s] \delta_m$ in Eqs. (2.2)–(2.3).

Next, we proceed to the third term of Eq. (2.8). This term arises from the difference in path length from the observer to the source between the straight line (along the r -axis) and the curved path (specified by λ) in Fig. 1. Substituting $d\mathbf{x}/d\lambda$ in Eq. (2.1) into Eq. (2.8), this term becomes

$$\begin{aligned} \Delta \text{DM}_{3\text{rd}}(z_s) &= \frac{2}{c^4} \int_0^{r_s} dr \bar{n}_e(z) (1+z) \left[\int_0^r dr' \int_0^r dr'' + \frac{1}{r_s^2} \int_0^{r_s} dr' (r_s-r') \int_0^{r_s} dr'' (r_s-r'') \right. \\ &\quad \left. - \frac{2}{r_s} \int_0^r dr' \int_0^{r_s} dr'' (r_s-r'') \right] \langle \nabla_{\mathbf{x}'} \phi(\mathbf{r}'; z') \cdot \nabla_{\mathbf{x}''} \phi(\mathbf{r}''; z'') \rangle \Big|_{\mathbf{x}'=\mathbf{x}''=0}. \end{aligned} \quad (\text{A.8})$$

Similar to Eq. (A.5), the correlation function of $\nabla_{\mathbf{x}} \phi$ in Eq. (A.8) is obtained as follows:

$$\langle \nabla_{\mathbf{x}'} \phi(\mathbf{r}'; z') \cdot \nabla_{\mathbf{x}''} \phi(\mathbf{r}''; z'') \rangle \Big|_{\mathbf{x}'=\mathbf{x}''=0} = \frac{9H_0^4 \Omega_m^2}{4} (1+z')^2 \int \frac{d^2 k_\perp}{(2\pi)^2} \frac{1}{k_\perp^2} P_m(k_\perp; z') \delta_D(r'-r''), \quad (\text{A.9})$$

where P_m is the matter power spectrum defined as $\langle \tilde{\delta}_m(\mathbf{k}'; z) \tilde{\delta}_m^*(\mathbf{k}; z) \rangle \equiv (2\pi)^3 \delta_D(\mathbf{k}-\mathbf{k}') P_m(k; z)$. Using Eq. (A.9), Eq. (A.8) is rewritten as

$$\Delta \text{DM}_{3\text{rd}}(z_s) = \int_0^{r_s} dr \bar{n}_e(z) (1+z) \int_0^r dr' \frac{2r'-r_s}{r_s} J(z') + \overline{\text{DM}}(z_s) \int_0^{r_s} dr \left(\frac{r_s-r}{r_s} \right)^2 J(z), \quad (\text{A.10})$$

with

$$J(z) = \frac{9H_0^4 \Omega_m^2}{4\pi c^4} (1+z)^2 \int_0^\infty \frac{dk_\perp}{k_\perp} P_m(k_\perp; z). \quad (\text{A.11})$$

The function $J(z)$ is the same as in KP16. The smallness of the dimensionless quantity rJ is discussed in Section 1.3 of KP16. The third term $\Delta \text{DM}_{3\text{rd}}$ is orders of magnitude smaller compared to the first and second terms in Eq. (2.8).

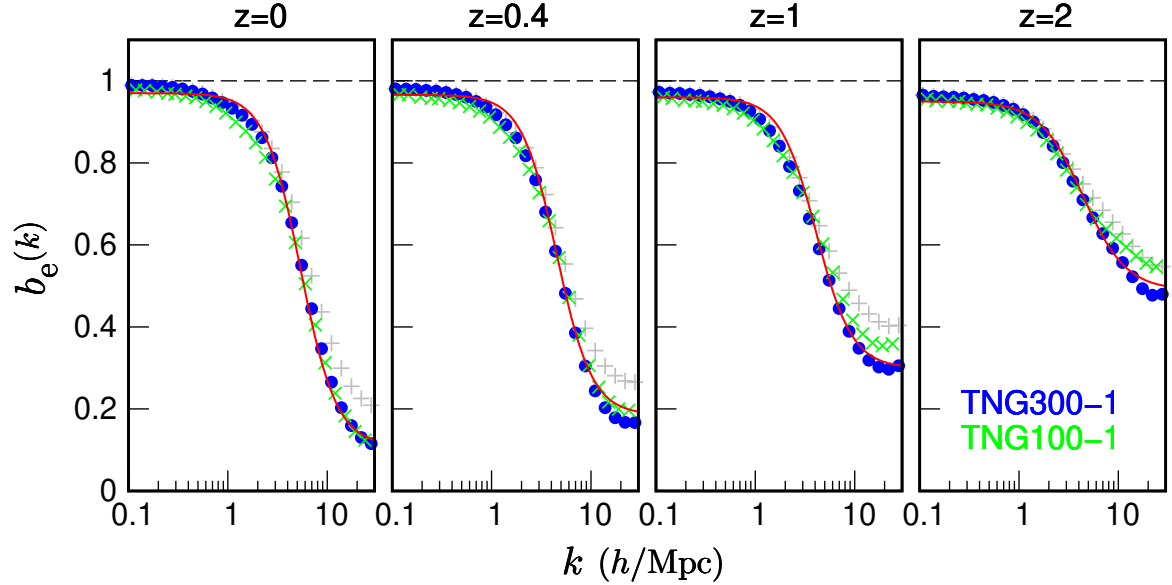


Figure 4. The free-electron bias is defined as the ratio of the cross-power spectrum $P_{\text{me}}(k)$ to the matter power spectrum in the DMO run $P_{\text{DMO}}(k)$: $b_e(k) \equiv P_{\text{me}}(k)/P_{\text{DMO}}(k)$. The blue and green symbols represent measurements in TNG300-1 and TNG100-1, respectively. The solid red curve is the fitting function (B.1). The gray pluses are the bias in our previous work [63], $b_e^{(\text{prev})}(k; z) \equiv [P_e(k; z)/P_{\text{DMO}}(k; z)]^{1/2}$, measured in TNG300-1.

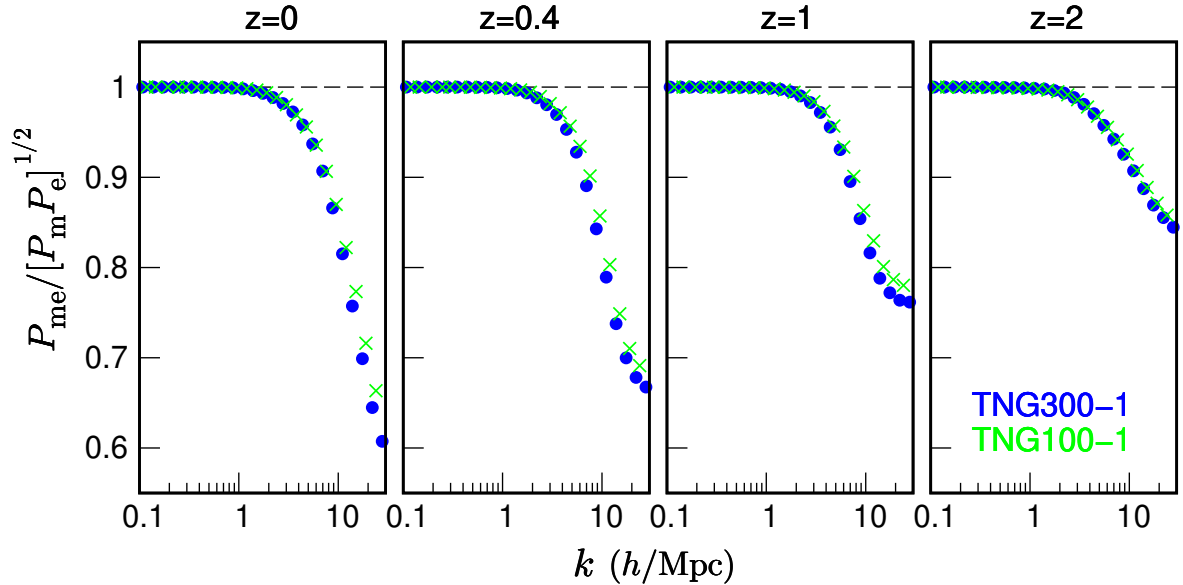


Figure 5. The cross-correlation coefficient is defined as $P_{\text{me}}(k)/[P_{\text{m}}(k)P_e(k)]^{1/2}$. The blue and green symbols represent measurements in TNG300-1 and TNG100-1, respectively.

B Free-electron bias

This section introduces a fitting function for the free-electron bias, defined as $b_e(k; z) \equiv P_{\text{me}}(k; z)/P_{\text{DMO}}(k; z)$, using TNG300-1 and TNG100-1. The fitting range is $k < 38.3 h \text{ Mpc}^{-1}$

and $76.2 h \text{ Mpc}^{-1}$ for TNG300-1 and TNG100-1 (i.e., the Nyquist wavenumbers), respectively, in $z = 0-3$ ($z = 0, 0.2, 0.4, 0.7, 1, 2$ and 3). Figure 4 shows the bias for $z = 0, 0.4, 1$ and 2 . The sample variance of the power spectrum, caused by the finite simulation volume, is canceled because the hydrodynamic run and the DMO run have the same initial seed of random Gaussian fluctuations. The bias is fitted as follows:

$$b_e(k; z) = \frac{b_0(z)}{1 + [k/k_*(z)]^\gamma} + b_1(z), \quad (\text{B.1})$$

with

$$\begin{aligned} b_0(z) &= 0.86 - 0.20z, \\ b_1(z) &= 0.11 + 0.19z, \\ k_*(z) &= 5.4 - 2.9z + 2.0z^2 - 0.40z^3, \\ \gamma(z) &= 2.4 + 0.2z - 0.2z^2, \end{aligned}$$

where k_* is in unit of $h \text{ Mpc}^{-1}$. The fitting function agrees with both simulations (TNG300-1 and TNG100-1) to within 4.3% (9.5%) for $k \leq 1$ (10) $h \text{ Mpc}^{-1}$ and $z = 0-3$. The bias approaches unity on large scales ($k \lesssim 1 h \text{ Mpc}^{-1}$), but is significantly reduced on small scales ($k \gtrsim 1 h \text{ Mpc}^{-1}$) owing to AGN and stellar feedback. The bias is slightly smaller than unity on the largest scales, especially for higher redshifts, because the fluctuations in baryons gradually catch up to the fluctuations in dark matter after the cosmological recombination (e.g., Subsection 3.3 of Ref. [63]).

It is worth noting that the free-electron bias differs slightly from the bias defined in our previous study [63] using the free-electron power spectrum P_e : $b_e^{(\text{prev})}(k; z) = [P_e(k; z) / P_{\text{DMO}}(k; z)]^{1/2}$. The gray pluses in Fig. 4 represent the previous bias. Both biases are nearly identical on large scales ($k \lesssim 1 h \text{ Mpc}^{-1}$), but the new one is slightly more suppressed at $k \gtrsim 1 h \text{ Mpc}^{-1}$. To view this difference from another perspective, the cross-correlation coefficient,

$$r(k; z) \equiv \frac{P_{\text{me}}(k; z)}{[P_{\text{m}}(k; z)P_e(k; z)]^{1/2}}, \quad (\text{B.2})$$

is plotted in Fig. 5. Here, P_{m} is the matter power spectrum of the hydrodynamic simulations (not the DMO simulations). The coefficient r quantifies the phase difference between the two fields. If the phases differ, such as when $\arg(\tilde{\delta}_e(\mathbf{k}; z)) - \arg(\tilde{\delta}_m(\mathbf{k}; z)) = \theta$ where θ is a constant, then $r = \cos \theta$. Alternatively, if $\tilde{\delta}_e(\mathbf{k}; z) = b_1(k; z) \tilde{\delta}_m(\mathbf{k}; z)$ with a real function b_1 , then $r = 1$. Figure 5 shows $r = 1$ for large scales ($k \lesssim 1 h \text{ Mpc}^{-1}$), but $r < 1$ for small scales ($k \gtrsim 1 h \text{ Mpc}^{-1}$). Here, $r < 1$ leads to additional small-scale suppression of b_e compared to $b_e^{(\text{prev})}$, as shown in Fig. 4.

Acknowledgments

We thank Kunihiro Ioka, Alex Mead, and Masamune Oguri for their helpful comments and suggestions. We thank the Enago (www.enago.jp) editors for the English language review. This work is supported in part by JSPS KAKENHI grant Nos. JP22H00130 and JP20H05855.